AAS 19-685

DESENSITIZED OPTIMAL SPACECRAFT RENDEZVOUS CONTROL WITH POORLY KNOWN GRAVITATIONAL AND SOLAR RADIATION PRESSURE PERTURBATIONS

Ethan R. Burnett[*], Andrew Harris[†], and Hanspeter Schaub[‡]

Robust rendezvous guidance is implemented in an environment with uncertain dominant gravitational harmonics C_{20} and C_{22} and poorly-known solar radiation pressure (SRP) effects. The rendezvous control design presumes the availability of a throttled low-thrust propulsion system, which can be achieved by pulsed plasma thrusters. The control minimizes an augmented cost function composed of the traditional Linear Quadratic Regulator (LQR) terms and terms that are quadratic in system sensitivity to multiple unknown dynamical parameters. Results show that there is much closer agreement between the linear designed trajectory and true controlled trajectory using the desensitized control strategy than there is for LQR.

INTRODUCTION

Uncertainty is a major obstacle to robust spacecraft control. In particular, while the physics of the space environment are often reasonably well understood, the true values of perturbative parameters are frequently poorly known. This is especially true in missions to previously unexplored or dynamically complex bodies. This can also still pose a challenge for more familiar environments with unpredictable variations, such as the constantly changing conditions of the rarefied atmosphere in low-Earth orbits. Controllers that are not designed to account for or be robust to uncertainty are fundamentally ill-suited for use in such space missions. An active area of research is design of controllers that are naturally robust to poorly-known dynamical parameters. Such controllers still typically use some nominal or expected values for these parameters, but are designed to be operationally desensitized to reasonable deviations from the expected values. Desensitized linear optimal control is one appealing option, due to its relative ease of design, analysis, and implementation. This method was first developed by Kahne[7] in the 1960s, and fundamentally similar methods have been applied in trajectory design[12] and optimal landing guidance.[13] Similar work has also been done in desensitized optimal filtering, in which the estimator is designed to be tolerant of poorly known dynamical parameters.[8] It is possible to develop desensitized control for the spacecraft relative motion problem, which enables more robust control design for rendezvous guidance and formation maintenance.

[*]Research Assistant, Ann and H.J. Smead Department of Aerospace Engineering Sciences, University of Colorado Boulder, Boulder, CO, 80309 USA.

[†]Research Assistant, Ann and H.J. Smead Department of Aerospace Engineering Sciences, University of Colorado Boulder, Boulder, CO, 80309 USA.

[‡]Glenn L. Murphy Chair of Engineering, Smead Department of Aerospace Engineering Sciences, University of Colorado, 431 UCB, Colorado Center for Astrodynamics Research, Boulder, CO 80309-0431. AAS Fellow, AIAA Fellow.

This paper implements a new approach to spacecraft relative motion Linear Quadratic Regulator (LQR) control in a highly uncertain environment, with a modification to design a linearly optimal controller that is minimally sensitive to chosen system perturbations, but otherwise inherits the traditional features of LQR control. This is done by extending the work originally presented by Kahne[7] to enable control design that is desensitized to variations in an arbitrary number of poorly known system dynamical parameters, and applying the method to spacecraft formation/rendezvous control.

As an example application, this paper is focused on control design in the highly perturbed environment around small asteroids, in which the gravitational harmonics C_{20} and C_{22} and solar radiation pressure (SRP) constitute the dominant perturbations for a range of orbits potentially desirable for future missions. The decision to truncate the gravitational effects at the second degree and order implicitly assumes that the spacecraft are in high orbits, where individual surface features and higher order gravity field components are dominated by the C_{20} and C_{22} perturbation. Third-body effects may also be important enough to warrant inclusion in the control design, in sufficiently high orbits. This work could be extended to apply in such an environment if the effects of the additional perturbation is accounted for, and the modification is conceptually straightforward.

The control design assumes that the gravitational harmonics are not well-known (such as if they are estimated from light curve data[6]). Uncertainty in the magnitude of the SRP force is also considered. The control model is first derived using the linearized dynamics containing linear perturbation terms due to gravity coefficients C_{20} and C_{22}, and the SRP force, and the controller is then applied in a nonlinear dynamic truth model with differing values of the chosen dynamical parameters to test the performance of the controller. This paper investigates the effect of these mis-modeled parameters on the control performance for both standard LQR and desensitized optimal control.

The work presented in this paper is directly relevant for mission design to small-body environments, in which after orbital insertion, it is desired to correct to a nominal orbit, maintain a nominal orbit under the presence of perturbations, or even facilitate spacecraft rendezvous in this uncertain environment. However, the given implementation can be easily adapted for robust rendezvous control in Earth orbits as well, and the procedure introduced in this paper can be readily adapted to minimize uncertainty to essentially any other poorly known dynamical parameters.

LINEARIZED RELATIVE MOTION MODELS FOR CONTROL

The approximate model is constructed in part using a model accounting for C_{20} and C_{22} recently obtained and tested in Reference 1. The additional linear perturbative terms due to SRP were more recently obtained.[2] To the knowledge of the authors, this is the only linear relative motion model that includes the significant perturbative effects of the C_{22} coefficient. The model is derived so that the perturbed behavior of the chief orbit is approximated by time-varying terms in the system matrix, and the kinematics of relative motion are derived with the effects of the perturbations rigorously accounted for.[3,4] This methodology yields models with far greater accuracy than models which add perturbative terms to the Clohessy-Wiltshire model in an ad-hoc manner.

Figure 1 shows the geometry of the spacecraft orbit. The axes $\hat{\boldsymbol{a}}_1, \hat{\boldsymbol{a}}_2, \hat{\boldsymbol{a}}_3$ are aligned with the principal axes of inertia of the asteroid, and the asteroid is assumed to be in a spin about the axis of maximum inertia. The spin axis is perpendicular to the inertially fixed plane from which the orbit is defined. The right ascension Ω is measured from an inertially fixed reference direction $\boldsymbol{\gamma}$ in this plane, along with the asteroid rotation angle $\psi = \psi_0 + ct$ tracking the $\hat{\boldsymbol{a}}_1$ vector. The vector

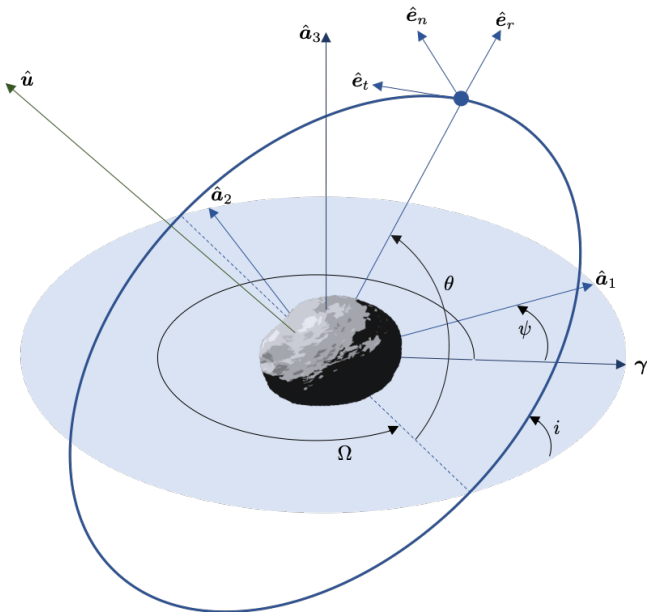

Figure 1. Problem Geometry

$\hat{\boldsymbol{u}}$ points towards the sun, and the plane perpendicular to this vector is the terminator plane. The relative motion problem is centered on a real or virtual chief spacecraft in a near-circular orbit, for which the argument of latitude $\theta = \omega + f$ is a convenient angular coordinate.

The dominant effects of the gravity field coefficients C_{20} and C_{22} are accounted for by the linearized model, along with the influence of SRP disturbances, using a body-averaged single-plate SRP model. These terms capture the most important effects for sufficiently high orbits around large asteroids.[11] The effects of the orbit geometry play an important role in the formation dynamics, but the assumptions $r \approx a_0$ and $\theta \approx \theta_0 + nt$ are appropriate for the time span of several orbits, where $n = \sqrt{\mu/a^3}$ is the unperturbed mean motion. The angular rate ratio is defined as $\Gamma = c/n$, R is the Brillouin sphere radius, φ is the asteroid argument of latitude, and h is the orbit angular momentum. The model is given below, in which the kinematics of the perturbed LVLH frame are well-approximated for several orbits, the orbit parameters a, i, and Ω are initialized with the initial values for the chief, and these perturbed chief orbit parameters may be updated as needed:

$$\begin{bmatrix} \ddot{x} \\ \ddot{y} \\ \ddot{z} \end{bmatrix} = n^2 \begin{bmatrix} F_{11} & F_{12} & F_{13} \\ F_{21} & F_{22} & F_{23} \\ F_{31} & F_{32} & F_{33} \end{bmatrix} \begin{bmatrix} x \\ y \\ z \end{bmatrix} + \begin{bmatrix} 0 & 2\omega_n & 0 \\ -2\omega_n & 0 & 2\omega_r \\ 0 & -2\omega_r & 0 \end{bmatrix} \begin{bmatrix} \dot{x} \\ \dot{y} \\ \dot{z} \end{bmatrix} \tag{1}$$

$$\begin{aligned} F_{11} = 3 &- \frac{3}{8} C_{20} \left(\frac{R}{a}\right)^2 \left[20\left(1 - 3\sin^2 i \sin^2\theta\right)\right] \\ &+ \frac{3}{8} C_{22} \left(\frac{R}{a}\right)^2 \Big[30\cos\left(2\left(\Omega - \psi\right)\right)\left(\left(3 + \cos 2i\right)\cos 2\theta + 2\sin^2 i\right) \\ &- 120\sin\left(2\left(\Omega - \psi\right)\right)\cos i \sin 2\theta\Big] \end{aligned} \tag{2a}$$

$$
\begin{aligned}
F_{12} = & -6C_{20}\left(\frac{R}{a}\right)^2 \sin^2 i \sin 2\theta + \frac{3}{4}C_{22}\left(\frac{R}{a}\right)^2 \Big[8\cos\left(2\left(\Omega-\psi\right)\right)\left(3+\cos 2i\right)\sin 2\theta \\
& +32\sin\left(2\left(\Omega-\psi\right)\right)\cos i\cos 2\theta\Big]
\end{aligned} \tag{2b}
$$

$$
\begin{aligned}
F_{13} = & -15\sin i\Bigg(C_{20}\left(\frac{R}{a}\right)^2 \cos i\sin\theta + 2C_{22}\left(\frac{R}{a}\right)^2 \Big[\cos\left(2\left(\Omega-\psi\right)\right)\cos i\sin\theta \\
& +\sin\left(2\left(\Omega-\psi\right)\right)\cos\theta\Big]\Bigg) - \frac{a}{nh}N_{\text{SRP}}
\end{aligned} \tag{2c}
$$

$$
F_{21} = F_{12} \tag{2d}
$$

$$
\begin{aligned}
F_{22} = & 3C_{20}\left(\frac{R}{a}\right)^2 \sin^2 i\cos 2\theta - \frac{3}{4}C_{22}\left(\frac{R}{a}\right)^2 \Big[4\cos\left(2\left(\Omega-\psi\right)\right)\left(3+\cos 2i\right)\cos 2\theta \\
& -16\sin\left(2\left(\Omega-\psi\right)\right)\cos i\sin 2\theta\Big]
\end{aligned} \tag{2e}
$$

$$
\begin{aligned}
F_{23} = & 6\sin i\Bigg(2C_{22}\left(\frac{R}{a}\right)^2 \Big[\cos\left(2\left(\Omega-\psi\right)\right)\left(\cos i-\Gamma\right)\cos\theta \\
& +\sin\left(2\left(\Gamma-\psi\right)\right)\left(\Gamma\cos i-1\right)\sin\theta\Big] + C_{20}\left(\frac{R}{a}\right)^2 \cos i\cos\theta\Bigg) + \frac{\dot{\varphi}}{n^2}\frac{a}{h}\frac{d}{d\varphi}\left(N_{\text{SRP}}\right)
\end{aligned} \tag{2f}
$$

$$
F_{31} = F_{13} \tag{2g}
$$

$$
\begin{aligned}
F_{32} = & 12C_{22}\left(\frac{R}{a}\right)^2 \Gamma\sin i\left(\cos\left(2\left(\Omega-\psi\right)\right)\cos\theta - \sin\left(2\left(\Omega-\psi\right)\right)\cos i\sin\theta\right) \\
& -\frac{\dot{\varphi}}{n^2}\frac{a}{h}\frac{d}{d\varphi}\left(N_{\text{SRP}}\right)
\end{aligned} \tag{2h}
$$

$$
\begin{aligned}
F_{33} = & -1 + \frac{1}{4}C_{20}\left(\frac{R}{a}\right)^2 \Big[6+12\cos^2 i - 30\sin^2 i\sin^2\theta\Big] \\
& +\frac{1}{4}C_{22}\left(\frac{R}{a}\right)^2 \Big[\cos\left(2\left(\Omega-\psi\right)\right)\left(-15\left(3+\cos 2i\right)\cos 2\theta - 54\sin^2 i\right) \\
& +60\sin\left(2\left(\Omega-\psi\right)\right)\cos i\sin 2\theta\Big]
\end{aligned} \tag{2i}
$$

The angular velocities of the perturbed LVLH frame are given below:

$$
\begin{aligned}
\omega_n = & n\Bigg(1 - \frac{3}{4}\left(\frac{R}{a}\right)^2 \Big[C_{20}\left(1-3\sin^2 i\sin^2\theta\right) + 6C_{22}\Big(\sin\left(2\left(\Omega-\psi\right)\right)\cos i\sin 2\theta \\
& -\frac{1}{4}\cos\left(2\left(\Omega-\psi\right)\right)\left(1+3\cos 2\theta - 2\cos 2i\sin^2\theta\right)\Big)\Big]\Bigg)
\end{aligned} \tag{3}
$$

$$
\begin{aligned}
\omega_r = & 3n\left(\frac{R}{a}\right)^2 \sin i\Big(2C_{22}\sin\left(2\left(\Omega-\psi\right)\right)\cos\theta + \left[C_{20}+2C_{22}\cos\left(2\left(\Omega-\psi\right)\right)\right]\cos i\sin\theta\Big) \\
& +\frac{a}{h}N_{\text{SRP}}
\end{aligned} \tag{4}
$$

The term N_{SRP} is the $\hat{\boldsymbol{e}}_n$ component of the SRP disturbance acceleration:

$$N_{\text{SRP}} = -P(R_O)\frac{A}{m}\left(\frac{(1-\overline{\rho s})}{C_{1(1,1)}} + \overline{a}_2 + 2\overline{\rho s}C_{1(1,1)}\right) C_{1(1,1)}\left(\hat{\boldsymbol{e}}_\xi^\top [C_1(\boldsymbol{\sigma}_r)]^\top \hat{\boldsymbol{e}}_1\right) \tag{5}$$

where $\hat{\boldsymbol{e}}_1 = [1,0,0]^\top$ and the unit vector $\hat{\boldsymbol{e}}_\xi$ is not a function of θ due to the problem geometry:

$$\hat{\boldsymbol{e}}_\xi = \begin{pmatrix} \sin\kappa\sin\varphi\cos i - \sin\Omega\cos\varphi\sin i + \cos\Omega\cos\kappa\sin\varphi\sin i \\ \sin\kappa\cos\varphi\cos i + \sin\Omega\sin\varphi\sin i + \cos\Omega\cos\kappa\cos\varphi\sin i \\ \cos\kappa\cos i - \cos\Omega\sin\kappa\sin i \end{pmatrix} \tag{6}$$

with solar radiation pressure terms defined below, for a single-plate model of a spacecraft:

$$P(R_O) \approx \frac{G_1}{R_O^2} \tag{7}$$

$$\overline{a}_2 = \overline{B}(1-\overline{s})\overline{\rho} + (1-\overline{\rho})\overline{B} \tag{8}$$

The function $P(R_O)$ is the solar radiation pressure at asteroid orbit distance R_O, and G_1 is the solar radiation force constant at 1 AU. The specular and diffuse reflectivity coefficients are $\overline{s}$ and $\overline{\rho}$, and $\overline{B}$ is the Lambertian scattering coefficient. The model implicitly assumes that the spacecraft orientation with respect to the sun does not change significantly and that the spacecraft orbits are near-circular. It also does not account for eclipse effects without modification.

The matrix $[C_1(\boldsymbol{\sigma}_r)]$ is the rotation matrix from the asteroid-centered Hill frame to the spacecraft reference orientation. The primary body Hill frame H_P is defined by orthonormal vectors $\left\{\hat{\boldsymbol{u}}, \hat{\boldsymbol{H}} \times \hat{\boldsymbol{u}}, \hat{\boldsymbol{H}}\right\}$, where $\hat{\boldsymbol{u}}$ points toward the sun and $\hat{\boldsymbol{H}}$ is out of the orbit plane of the primary body. In all cases studied here, $[C_1(\boldsymbol{\sigma}_r)] = [I_{3\times 3}]$ and thus $C_{1(1,1)} = 1$ (sun-facing). The angle κ is the obliquity of the ecliptic plane and φ is the argument of latitude, or the rotation angle (in the orbit plane) from the Vernal Equinox to the radial vector from the sun to the planet. This model is derived from the facet-based SRP model given by McMahon and Scheeres,[9,10] and is suitable for on-board use. The model assumes that the asteroid is in a circular orbit about the sun, but this could be updated without great difficulty. The timescale of large variations in φ is very slow compared to the orbit period.

LOW-SENSITIVITY OPTIMAL CONTROL DESIGN

A method of improved optimal control design is introduced, which minimizes the effect of mismodeled parameters by augmenting in the sensitivities to these parameters to the cost function:

$$J = \frac{1}{2}\boldsymbol{x}^\top(t_f)[S]\boldsymbol{x}(t_f) + \frac{1}{2}\int_0^{t_f}\left(\boldsymbol{x}^\top(t)[Q(t)]\boldsymbol{x}(t) + \boldsymbol{u}^\top(t)[R(t)]\boldsymbol{u}(t) + \boldsymbol{s}^\top(t)[E(t)]\boldsymbol{s}(t)\right)dt \tag{9}$$

where $[E]$ is the weight matrix associated with the sensitivity cost and $\boldsymbol{s}(t)$ is the sensitivity vector:

$$\boldsymbol{s}(t) = \left.\frac{\mathrm{d}\boldsymbol{x}(t)}{\mathrm{d}\alpha}\right|_{\alpha_{nom}} \tag{10}$$

and it can be shown to obey

$$\dot{\boldsymbol{s}}(t) = [A(t)]\boldsymbol{s}(t) + [C(t)]\boldsymbol{x}(t) \tag{11}$$

where $[C(t)]_{ij} = \left.\frac{d[A]_{ij}}{d\alpha}\right|_{\alpha_{\text{nom}}}$. This elegant modification of the LQR optimal control problem was first performed by Kahne.[7] In order to use this technique to apply to a control problem with three poorly-known parameters, two additional sensitivity vector terms must be added to the cost function, and the same procedure will be followed to derive the modified equations for optimal control that minimizes the controlled trajectory sensitivity to three parameters.

Now, Kahne's procedure is extended to optimal linear control with an arbitrary number of sensitivity vectors augmented into the cost function:

$$J = \frac{1}{2}\boldsymbol{x}^\top(t_f)[S]\boldsymbol{x}(t_f) + \frac{1}{2}\int_0^{t_f}\left(\boldsymbol{x}^\top(t)[Q(t)]\boldsymbol{x}(t) + \boldsymbol{u}^\top(t)[R(t)]\boldsymbol{u}(t) + \sum_{i=1}^{p}\boldsymbol{s}_i^\top(t)[E_i(t)]\boldsymbol{s}_i(t)\right)dt \tag{12}$$

where $\boldsymbol{s}_i(t)$ is the i$^{\text{th}}$ sensitivity vector:

$$\boldsymbol{s}_i(t) = \left.\frac{\mathrm{d}\boldsymbol{x}(t)}{\mathrm{d}\alpha_i}\right|_{\alpha_{i,\text{nom}}} \tag{13}$$

$$\dot{\boldsymbol{s}}_i(t) = [A(t)]\boldsymbol{s}_i(t) + [C_i(t)]\boldsymbol{x}(t) \tag{14}$$

$$[C_{i(jk)}(t)] = \left.\frac{\partial[A_{jk}(t)]}{\partial\alpha_i}\right|_{\alpha_{i,\text{nom}}} \tag{15}$$

The Hamiltonian is given below:

$$H = \frac{1}{2}\left(\boldsymbol{x}^\top[Q]\boldsymbol{x} + \boldsymbol{u}^\top[R]\boldsymbol{u} + \sum_i \boldsymbol{s}_i^\top[E_i]\boldsymbol{s}_i\right) + \boldsymbol{\lambda}^\top\left([A]\boldsymbol{x} + [B]\boldsymbol{u}\right) + \sum_i \boldsymbol{q}_i^\top\left([A]\boldsymbol{s}_i + [C_i]\boldsymbol{x}\right) \tag{16}$$

The necessary conditions for optimality yield the following:

$$\dot{\boldsymbol{x}} = \frac{\partial H}{\partial \boldsymbol{\lambda}} = [A]\boldsymbol{x} + [B]\boldsymbol{u} \tag{17}$$

$$\dot{\boldsymbol{\lambda}} = -\frac{\partial H}{\partial \boldsymbol{x}} = -[Q]\boldsymbol{x} - [A]^\top\boldsymbol{\lambda} - \sum_i [C_i]^\top\boldsymbol{q}_i \tag{18}$$

$$\dot{\boldsymbol{s}}_i = \frac{\partial H}{\partial \boldsymbol{q}_i} = [A]\boldsymbol{s}_i + [C_i]\boldsymbol{x} \tag{19}$$

$$\dot{\boldsymbol{q}}_i = -\frac{\partial H}{\partial \boldsymbol{s}_i} = -[E_i]\boldsymbol{s}_i - [A]^\top\boldsymbol{q}_i \tag{20}$$

$$\frac{\partial H}{\partial \boldsymbol{u}} = [R]\boldsymbol{u} + [B]^\top\boldsymbol{\lambda} = \boldsymbol{0} \;\rightarrow\; \boldsymbol{u}(t) = -[R]^{-1}[B]^\top\boldsymbol{\lambda}(t) \tag{21}$$

The split final and initial conditions are $\boldsymbol{x}(0) = \boldsymbol{x}_0$, $\boldsymbol{\lambda}(t_f) = [S]\boldsymbol{x}(t_f)$, $\boldsymbol{s}_i(0) = \boldsymbol{0}$, $\boldsymbol{q}_i(t_f) = \boldsymbol{0}$.

To adapt the matrix/vector notation to an arbitrary number (p) of sensitivities, the augmented vector notation $\boldsymbol{s}_{p\times 1} = (\boldsymbol{s}_1^\top, \boldsymbol{s}_2^\top, \ldots, \boldsymbol{s}_p^\top)$ is defined, along with necessary augmented matrix notation given below:

$$[C_{6p\times 6}] = \begin{bmatrix}[C_1]\\ [C_2]\\ \vdots\\ [C_p]\end{bmatrix},\; [C_{6p\times 6}]^\top = \begin{bmatrix}[C_1]^\top & [C_2]^\top & \ldots & [C_p]^\top\end{bmatrix} \tag{22}$$

$$[A_{6p\times 6p}] = \begin{bmatrix} [A] & [0_{6\times 6}] & \cdots \\ [0_{6\times 6}] & \ddots & \\ \vdots & & [A] \end{bmatrix} \tag{23}$$

The augmented system dynamics are given below:

$$\begin{pmatrix} \dot{\boldsymbol{x}} \\ \dot{\boldsymbol{s}}_{6p\times 1} \\ \dot{\boldsymbol{\lambda}} \\ \dot{\boldsymbol{q}}_{6p\times 1} \end{pmatrix} = \begin{bmatrix} [A] & [0_{6\times 6p}] & -[B][R]^{-1}[B]^\top & [0_{6\times 6p}] \\ [C_{6p\times 6}] & [A_{6p\times 6p}] & [0_{6p\times 6}] & [0_{6p\times 6p}] \\ -[Q] & [0_{6\times 6p}] & -[A]^\top & -[C_{6p\times 6}]^\top \\ [0_{6p\times 6}] & -[E_{6p\times 6p}] & [0_{6p\times 6}] & -[A_{6p\times 6p}]^\top \end{bmatrix} \begin{pmatrix} \boldsymbol{x} \\ \boldsymbol{s}_{6p\times 1} \\ \boldsymbol{\lambda} \\ \boldsymbol{q}_{6p\times 1} \end{pmatrix} \tag{24}$$

Let $\boldsymbol{z} = \left(\boldsymbol{x}^\top, \boldsymbol{s}_{6p\times 1}^\top\right)$, $\boldsymbol{\psi} = \left(\boldsymbol{\lambda}^\top, \boldsymbol{q}_{6p\times 1}^\top\right)$, thus:

$$\begin{pmatrix} \dot{\boldsymbol{z}} \\ \dot{\boldsymbol{\psi}} \end{pmatrix} = [\Gamma(t)] \begin{pmatrix} \boldsymbol{z} \\ \boldsymbol{\psi} \end{pmatrix} \tag{25}$$

where $[\Gamma(t)]$ is the system matrix in Eq. (24). The solution to this system is given in terms of its STM:

$$\begin{pmatrix} \boldsymbol{z}(t) \\ \boldsymbol{\psi}(t) \end{pmatrix} = [\Phi(t, t_0)] \begin{pmatrix} \boldsymbol{z}(t_0) \\ \boldsymbol{\psi}(t_0) \end{pmatrix} \tag{26}$$

$$\boldsymbol{z}(t_f) = [\phi_{11}(t_f, t_0)]\boldsymbol{z}(t_0) + [\phi_{12}(t_f, t_0)]\boldsymbol{\psi}(t_0) \tag{27}$$

$$\boldsymbol{\psi}(t_f) = [\phi_{21}(t_f, t_0)]\boldsymbol{z}(t_0) + [\phi_{22}(t_f, t_0)]\boldsymbol{\psi}(t_0) = [S]\boldsymbol{x}(t_f) = [G]\boldsymbol{z}(t_f) \tag{28}$$

where $[G]$ is of dimension $6(p+1) \times 6(p+1)$, with all entries zero except the 6×6 upper left sub-matrix, $[S]$. Thus:

$$\boldsymbol{\psi}(t_f) = G\left([\phi_{11}(t_f, t)]\boldsymbol{z}(t) + [\phi_{12}(t_f, t)]\boldsymbol{\psi}(t)\right) \tag{29}$$

$$\boldsymbol{\psi}(t) = \left([\phi_{22}(t_f, t)] - [G][\phi_{12}(t_f, t)]\right)^{-1}\left([G][\phi_{11}(t_f, t)] - [\phi_{21}(t_f, t)]\right)\boldsymbol{z}(t) \equiv [K(t)]\boldsymbol{z}(t) \tag{30}$$

Applying the final conditions, it can be shown that $[K(t_f)] = [G]$. Partitioning $[K]$ into appropriately dimensioned sub-matrices, the top 6 rows of Eq. (30) are isolated:

$$\boldsymbol{\lambda}(t) = [K_{11}(t)]\boldsymbol{x}(t) + [K_{12}(t)]\boldsymbol{s}_{6p\times 1}(t) \tag{31}$$

The control signal is given in terms of the usual state feedback term, and a new feedback term for the augmented sensitivities:

$$\boldsymbol{u}(t) = -[R]^{-1}[B]^\top[K_{11}(t)]\boldsymbol{x}(t) - [R]^{-1}[B]^\top[K_{12}(t)]\boldsymbol{s}_{6p\times 1}(t) \tag{32}$$

Thus, $[K_{12}(t)]$ is a $6 \times 6p$ matrix that maps the augmented sensitivity vectors, and the differential equation for the full $[K]$ matrix will now be derived. First, differentiating Eq. (30), and isolating then rewriting the differential equations from the augmented dynamics:

$$\dot{\boldsymbol{\psi}} = [\dot{K}(t)]\boldsymbol{z}(t) + [K(t)]\dot{\boldsymbol{z}}(t) \tag{33}$$

$$\dot{\boldsymbol{z}}(t) = [L(t)]\boldsymbol{z}(t) - [M(t)]\boldsymbol{\psi}(t) \tag{34}$$

$$\dot{\boldsymbol{\psi}}(t) = -[N(t)]\boldsymbol{z}(t) - [P(t)]\boldsymbol{\psi}(t) \tag{35}$$

The new matrices in Eqs. (34) and (35) are directly obtained from the partitioned sub-matrices in Eq. (24) using the following definition:

$$[\Gamma(t)] = \begin{bmatrix} [L(t)] & -[M(t)] \\ -[N(t)] & -[P(t)] \end{bmatrix} \tag{36}$$

Using Eq. (30) in Eq. (34):

$$\dot{\boldsymbol{z}}(t) = ([L(t)] - [M(t)][K(t)])\, \boldsymbol{z}(t) \tag{37}$$

Eq. (37) is substituted into Eq. (33):

$$\dot{\boldsymbol{\psi}} = \Big([\dot{K}(t)] + [K(t)][L(t)] - [K(t)][M(t)][K(t)]\Big)\, \boldsymbol{z}(t) \tag{38}$$

Then, substituting Eq. (30) in Eq. (35), equating with (38) and rearranging:

$$\Big([\dot{K}(t)] + [K(t)][L(t)] + [P(t)][K(t)] - [K(t)][M(t)][K(t)] + [N(t)]\Big)\, \boldsymbol{z}(t) = \mathbf{0} \tag{39}$$

The ODE for $[K(t)]$ is given below, for which the final condition is $[K(t_f)] = [G]$, or equivalently $[K_{11}(t_f)] = [S]$, $[K_{12}(t_f)] = [0_{6\times 6p}]$, $[K_{21}(t_f)] = [0_{6p\times 6}]$, $[K_{22}(t_f)] = [0_{6p\times 6p}]$.

$$[\dot{K}(t)] + [K(t)][L(t)] + [P(t)][K(t)] - [K(t)][M(t)][K(t)] + [N(t)] = \mathbf{0} \tag{40}$$

Since $[K(t)]$ is symmetric, it is clear that not all elements of the matrix need to be numerically integrated. Eq. (40) is expanded and symmetry is used to obtain a smaller set of equations to be integrated, which will result in greater computational efficiency:

$$\begin{aligned}
&[\dot{K}_{11}] + [K_{11}][A] + [K_{12}][C_{6p\times 6}] + [A]^\top [K_{11}] + [C_{6p\times 6}]^\top [K_{12}]^\top - [K_{11}][B][R]^{-1}[B]^\top [K_{11}] \\
&+ [Q] = [0_{6\times 6}] \\
&[\dot{K}_{12}] + [K_{12}][A_{6p\times 6p}] + [A]^\top [K_{12}] + [C_{6p\times 6}]^\top [K_{22}] - [K_{11}][B][R]^{-1}[B]^\top [K_{12}] = [0_{6\times 6p}] \\
&[\dot{K}_{22}] + [K_{22}][A_{6p\times 6p}] + [A_{6p\times 6p}]^\top [K_{22}] - [K_{12}]^\top [B][R]^{-1}[B]^\top [K_{12}] + [E_{6p\times 6p}] = [0_{6p\times 6p}]
\end{aligned} \tag{41}$$

If the symmetry of $[K]$ is used, then one must solve $18p^2 + 39p + 21$ coupled scalar ODE equations to model the behavior of $[K]$. If the symmetry is not exploited, the number of equations to be solved is $36p^2 + 72p + 36$. This becomes more costly as more sensitivity vectors are added to the cost function, but this problem is still tractable for two uncertain parameters.

To implement this controller, Eq. (41) should be solved backwards in time from the given final conditions, to obtain a pre-saved gain schedule. Then, the control should be applied as shown in Eq. (32), where the signals $\boldsymbol{s}_{6p\times 1}$ are obtained by integrating $\dot{\boldsymbol{s}}_i(t) = [A(t)]\boldsymbol{s}_i(t) + [C_i(t)]\boldsymbol{x}(t)$ as the system evolves. Lastly, remaining error due to nonlinearity or neglected dynamics can be greatly reduced by feeding back an error integral term. Note that if one sets $[E_{6p\times 6p}] = [0_{6p\times 6p}]$, the effects of system sensitivity are ignored, and the problem reduces to standard LQR with a final cost.

NOTES ON SYSTEM NONLINEARITY AND ORBITING ASTEROIDS

Before simulating LQR control and low-sensitivity control in the highly perturbed asteroid orbit environment, this section discusses several necessary topics, which provide justification for the methods, analysis, and results that will follow.

Quantifying Nonlinearity

In general, successful application of the linear control law to the nonlinear system is limited to a finite region of space around the virtual chief, and to a finite span of time for which the assumptions of the linearized model hold. This region of space and span of time will be referred to as the linear regime. The amount of acceptable nonlinearity will differ depending on the application, and thus so will this definition. In this paper, the scale of system nonlinearity is quantified with a dimensionless index that represents the average spatial deviation between the linearized and nonlinear propagated dynamics:

$$\nu_s(t,t_0) = \frac{1}{t-t_0}\int_{t_0}^{t} \frac{\|\Delta \boldsymbol{r}_{nl}(\tau) - \Delta \boldsymbol{r}_l(\tau)\|}{\|\Delta \boldsymbol{r}_l(\tau)\|} d\tau \tag{42}$$

where $\Delta \boldsymbol{r} = [x, y, z]^\top$ and the velocity differentials do not need to be directly included in this index. This can be applied to results from both the uncontrolled dynamics and controlled dynamics, however the scale of this parameter can be expected to differ with these two implementations. This parameter may be a misleading representation if $\Delta \boldsymbol{r}_l \approx \mathbf{0}$ for much of the time range. This should be addressed by de-weighting or excluding such instances from the calculation of this quantity. Alternative nonlinearity measures may also be considered, such as the average spatial distance between the two trajectories:

$$e_s(t,t_0) = \frac{1}{t-t_0}\int_{t_0}^{t} \|\Delta \boldsymbol{r}_{nl}(\tau) - \Delta \boldsymbol{r}_l(\tau)\| d\tau \tag{43}$$

Orbit Control around Asteroids

Orbiting around asteroids is not always possible, because these bodies are small enough that solar radiation pressure can easily dominate the gravitational force. Furthermore, the gravitational perturbations due to non-sphericity are often quite large. It is important to bear in mind that orbital motion around asteroids is highly non-Keplerian – complex and chaotic. Despite the complexity, several assumptions about the asteroid and spacecraft are used in this paper to enable a study of near-optimal guidance in this environment.

The simulations in this paper use a hypothetical asteroid given in Table 1. The hypothetical asteroid is rather large, and its size makes orbits possible despite the effects of SRP and third body gravity disturbances. Sufficiently large asteroids tend to have shapes that are well-approximated by ellipsoids. In this case, the scale and effects of higher order gravity field components can be shown to be quite small for high orbits in comparison to C_{20} and C_{22}.[1]

The SRP disturbance on the spacecraft is assumed to be well-modeled by a simple flat-plate model. In this paper, it is also assumed to be sun-facing. Since most spacecraft are solar powered, and these panels constitute the majority of the projected surface area, this will often be a reasonable assumption.

The simulations assume that the orientation of the asteroid spin axis, its rotation period, and its gravitational parameter μ are well-known. The first two parameters could be well-estimated by camera data before rendezvous, while the third would be estimated from telemetry data from the initial encounter and orbit insertion. It is possible to extend the methods in this paper to account for uncertainty in these parameters as well.

The desired formation chief orbit to rendezvous with is initially a near-circular orbit in the terminator plane. The nominal initial target orbit for the survey phase of the OSIRIS-REx mission

is one such orbit. These orbits are naturally quasi-stable, and are an attractive target for initial orbit-targeting maneuvers.[5] However, the highly perturbed and uncertain environment can and will introduce error. The scenario studied in this paper is analogous to correcting post-maneuver orbit error with LQR control, using very low thrust.

Lastly, the formation flying rendezvous control problem presumes that the relative position and velocity of the spacecraft are sufficiently well-known, otherwise the rendezvous would not be attempted. The accuracy of knowledge of the chief orbit is less important. In fact, the desensitized control strategy could be implemented with the initial chief orbit elements chosen as the uncertain parameters. This would enable rendezvous control for a formation whose absolute position is somewhat uncertain, but for which the formation geometry is known from sensors on the individual spacecraft.

LOW-THRUST CONTROL SIMULATIONS

To test the various optimal control strategies, consider the case of the hypothetical asteroid in Table 1 and the initial conditions given in Table 3. First, LQR control is tested – in which it is assumed that the SRP and second-order gravitational parameters are accurately known. Then, low-sensitivity optimal control is implemented, and the results from these two strategies are compared. The repeated control parameters (used in both cases) are given in Table 2. The initial conditions are given in Table 3.

Table 1. Asteroid Simulation Physical Parameters

Parameters	Values
Asteroid semi-axes, C_{20} & C_{22}	$A = 6$, $B = 3$, $C = 2.5$, $C_{20} = -0.093$, $C_{22} = 0.0375$
Density, gravitational parameter	$\rho = 2.6$ g/cm^3, $\mu = 3.271 \times 10^4$ m^3/s^2
Asteroid spin axis, orientation	$T_r = 38.5$ hours, $\psi_0 = \pi/8$, $\kappa = 15^\circ$
Asteroid orbit	$e = 0$, $R = 2.4$ AU, $\theta_0 = \omega + f_0 = \pi/2$
Spacecraft optical properties	$\frac{A}{m} = 0.3$, $\overline{B} = 0.6$, $\overline{s} = 0.25$, $\overline{\rho} = 0.3$

Table 2. Recurring Control Parameters for LQR and Low-Sensitivity Cases

Parameter	Value
$[Q]$	$[Q] = 0_{6\times6}$
$[R]$	$(1 \times 10^{12})I_{3\times3}$
$[S_f]$	$S_f(1:3,1:3) = I_{3\times3}$, $S_f(4:6,4:6) = (1 \times 10^9)I_{3\times3}$
$[B]$	$B(1:3,1:3) = 0_{3\times3}$, $B(4:6,1:3) = I_{3\times3}$
$[E]$	$[E_1] = [E_2] = 0.1I_{6\times6}$, $[E_3] = 0.01I_{6\times6}$
$t_0, \Delta t, t_f$	$t_0 = 0, \Delta t = 200, t_f = 555800$ (2 orbits, 6.43 days)

Table 3. Simulation Initial Conditions - Controlled Motion

Parameters	Values
Chief Orbit Elements	$\mathbf{oe}_c = [a, e, i, \omega, \Omega, f_0] = [40 \text{ km}, 5 \times 10^{-4}, 75^\circ, 0^\circ, 0^\circ, 0^\circ]$
Deputy Orbit Element Differences	$\Delta\mathbf{oe} = \mathbf{oe}_d - \mathbf{oe}_c = [0 \text{ km}, 0.07, 2.0^\circ, 0^\circ, 0^\circ, 0^\circ]$
Initial Conditions (LVLH)	$\Delta\boldsymbol{r} = -2800\hat{\boldsymbol{e}}_x$ m, $\Delta\boldsymbol{v} = 0.1285\hat{\boldsymbol{e}}_y + 0.0339\hat{\boldsymbol{e}}_z$ m/s

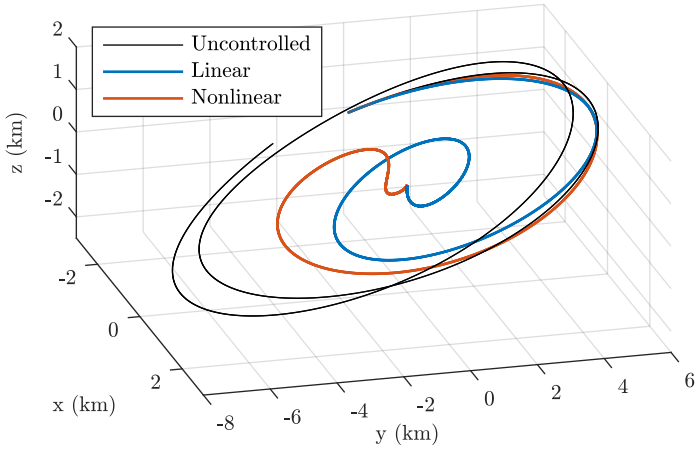

Figure 2. Controlled Relative Motion (LQR)

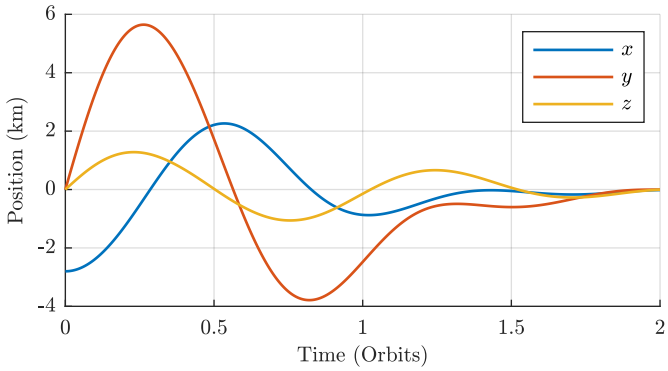

Figure 3. Relative Position vs. Time (LQR)

LQR Control

In this case, $[Q] = [0_{6\times6}]$ and it is the final state cost that drives the system to the origin. In Figure 2, it is clear that there is significant deviation between the control applied to the linear and nonlinear dynamics. Figure 3 shows the relative position vs. time from the control applied to the nonlinear dynamics. Since the LQR control is implemented by solving the matrix Riccati equation for $[K(t)]$ and feeding back $\boldsymbol{u}(t) = -[R]^{-1}[B]^{\top}[K(t)]\boldsymbol{x}(t)$, the deviations do not result in significant final miss distance. This closed-loop control implementation method seems naturally robust, at least in achieving the desired final condition. However, the significant deviation between the designed and actual controlled trajectories indicates that the effect of nonlinearities is non-negligible. This is also clear from the deviation between the designed (L) and actual (NL) control signals in Figure 4.

The positional sensitivity associated with C_{20}, C_{22}, and SRP force uncertainty are given in Figures 5 - 7. These results were propagated using Eq. (14) evaluated along the linear and nonlinear trajectories. These results indicate that while the SRP perturbation is largest, it is uncertainty in C_{22} that would result in the greatest deviation from the planned relative motion trajectory. This emphasizes the dynamic importance of C_{22} on relative motion dynamics in the asteroid orbit.

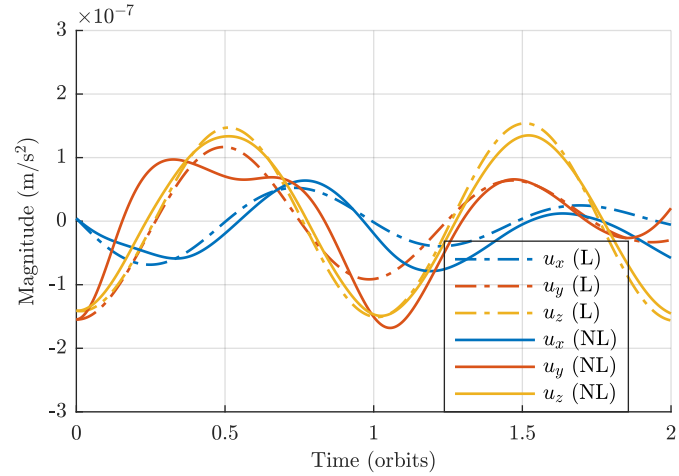

Figure 4. Control Signals (LQR)

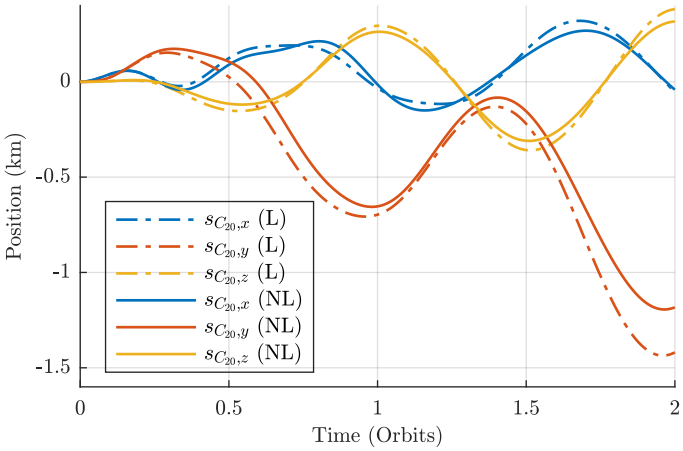

Figure 5. C_{20} Relative Position Sensitivity (LQR)

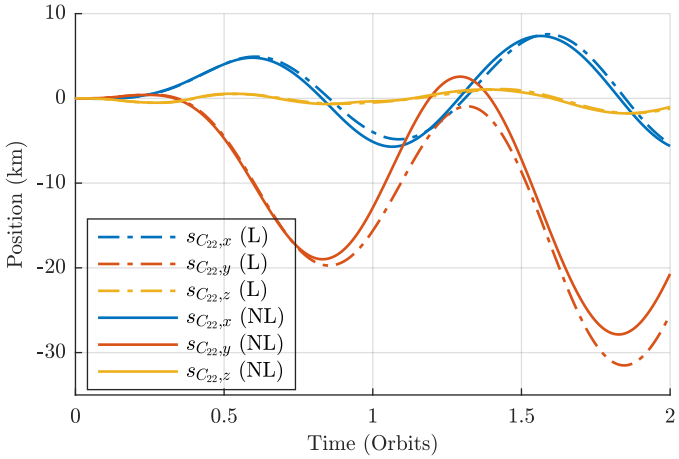

Figure 6. C_{22} Relative Position Sensitivity (LQR)

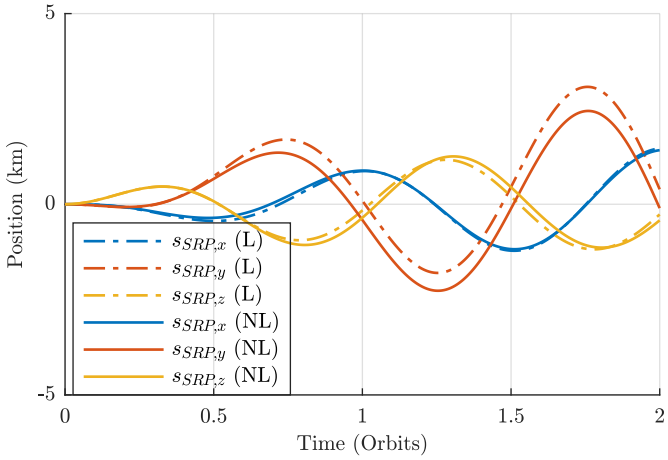

Figure 7. SRP Relative Position Sensitivity (LQR)

Low-Sensitivity Control

For the low-sensitivity control design, the control parameters given in Table 2 are unchanged. The sensitivity-associated weight matrices are for C_{20}, C_{22}, and SRP, respectively $E_1 = E_2 = 0.1I_{6\times6}$, and $E_3 = 0.01I_{6\times6}$. The control applied to the nonlinear dynamics is very close to the control applied to the linear dynamics. This is evident by comparing the linear and nonlinear results in Figures 8 and 10. The controller comes quite close to achieving the desired final condition. In addition, it is clear that the sensitivities to the three parameters are greatly reduced from the standard LQR results, which can be seen by comparing Figures 11 - 13 with Figures 5 - 7. Note that the y axis limits are greatly reduced for Figures 11 - 13.

It is worth noting that using poor values for the gravitational coefficients and SRP magnitude will not cause significant change to the trajectory design or control signals, which makes some intuitive sense. To minimize sensitivity to the poorly modeled parameters, the controller sends the deputy spacecraft on a trajectory whose design is minimally sensitive to errors in these parameters. Interestingly, this seems to result in a more close agreement between the control applied to the linear and nonlinear dynamics – suggesting that this control method should effectively expand the size of the linear regime. The effect of mis-modeled and unmodeled parameters on standard LQR control and low-sensitivity control is explored more fully by Monte Carlo analysis in the next section.

In general, this study illustrates that the shape of these low-sensitivity controlled trajectories are quite unintuitive and interesting. It also seems that they generally require more control than the traditional LQR design, compare Figures 10 and 4, but the required control is quite small (at or below the thrust level of small ion thrusters) in either case for station-keeping or formation control around this asteroid.

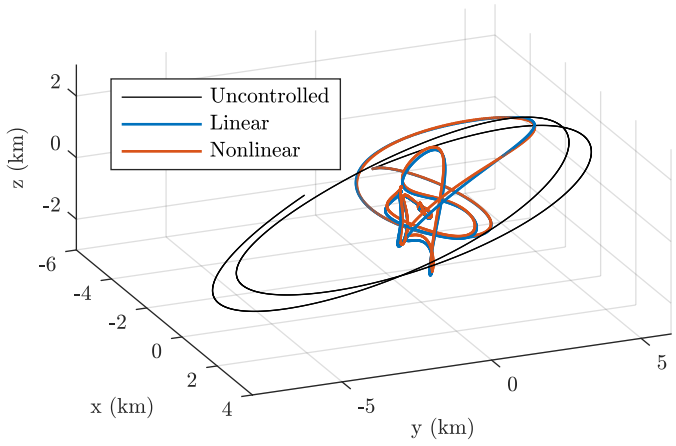

Figure 8. Controlled Relative Motion (Low-Sensitivity Control)

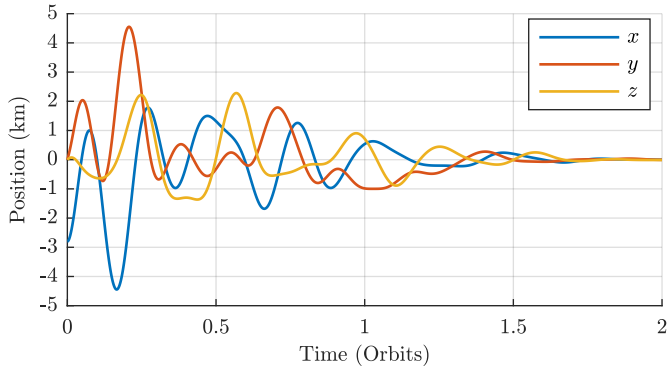

Figure 9. Relative Position vs. Time (Low-Sensitivity Control)

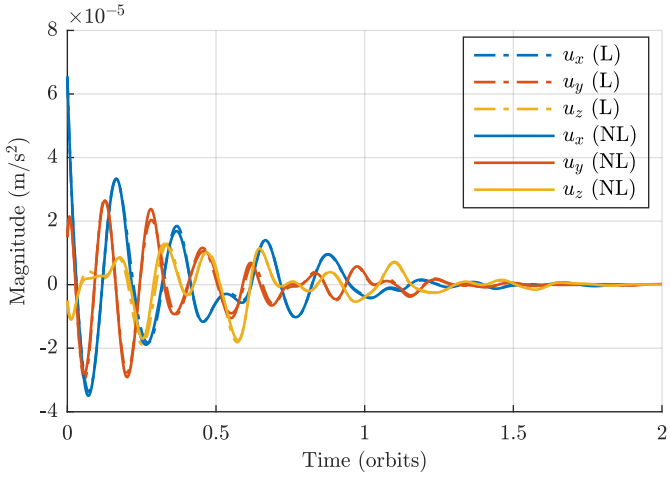

Figure 10. Control Signals (Low-Sensitivity Control)

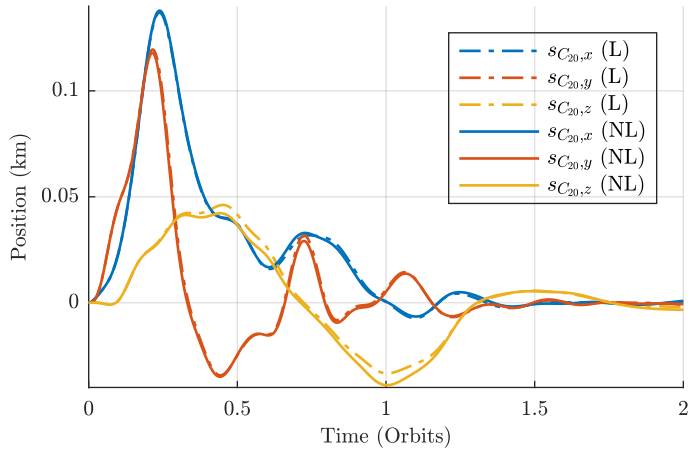

Figure 11. C_{20} Relative Position Sensitivity (Low-Sensitivity Control)

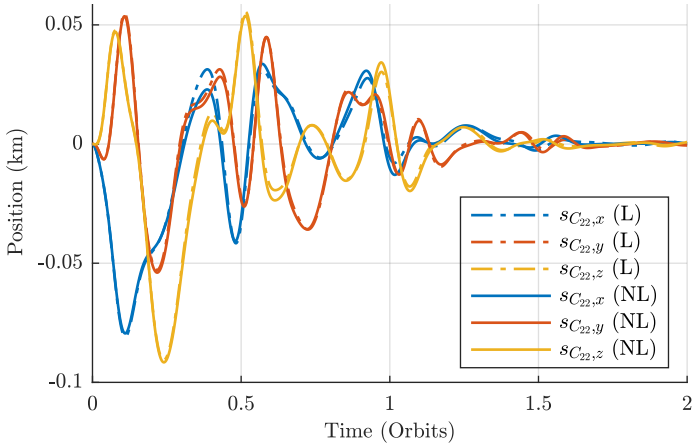

Figure 12. C_{22} Relative Position Sensitivity (Low-Sensitivity Control)

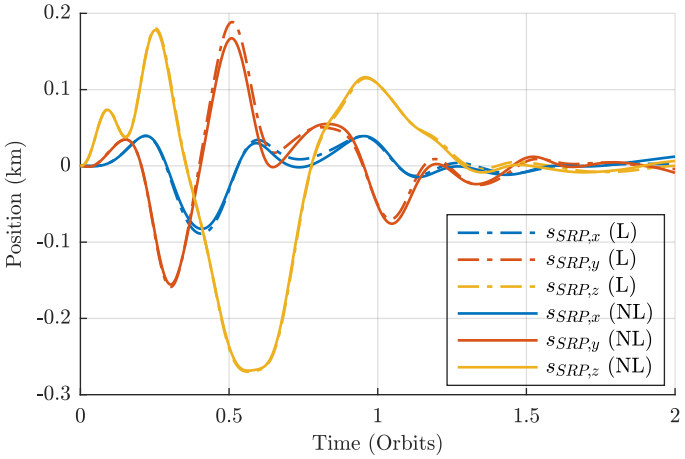

Figure 13. SRP Relative Position Sensitivity (Low-Sensitivity Control)

MONTE CARLO SIMULATIONS USING LOW-THRUST

In this section, Monte Carlo simulations of 50 runs were performed for both the standard LQR and the low-sensitivity control design from the previous section. All simulation parameters are reused, except the simulations now assume mis-modeled C_{20} and C_{22} with a 30% standard deviation about the nominal computed values, along with mis-modeled SRP force with a 20% standard deviation in magnitude from the expected value.

Figure 14 shows the controlled trajectories using standard LQR, and Figure 15 shows the controlled trajectories using low-sensitivity control. It is clear that both controllers successfully reach the origin of the LVLH frame. However, the LQR controller consistently deviates greatly from the trajectory predicted from the controlled linear dynamics given by the black line, while the low-sensitivity controller does not deviate much from the behavior predicted by the linearized model. Furthermore, the true low-sensitivity trajectories are spatially closer together than the true LQR trajectories, as would be expected.

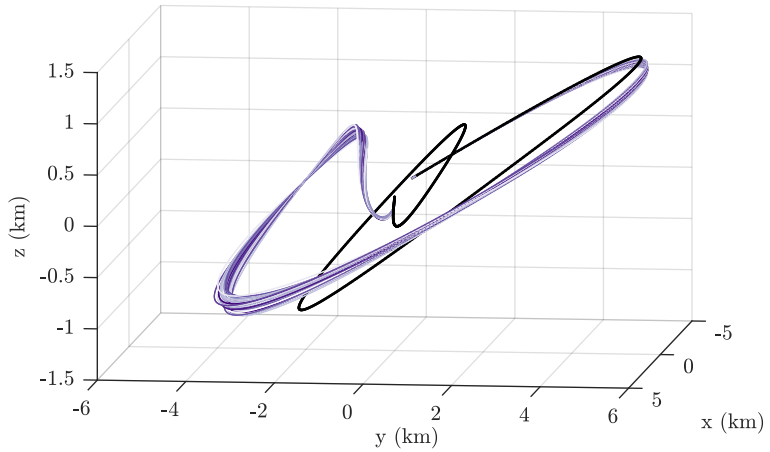

Figure 14. Controlled Relative Motion, Monte Carlo Results (LQR)

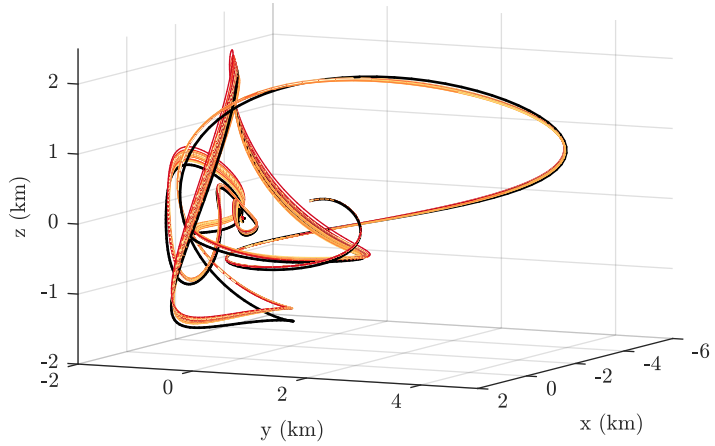

Figure 15. Controlled Relative Motion, Monte Carlo Results (Low-Sensitivity Control)

Figures 16 and 17 show the distributions of total Δv used by both controllers. The cost is higher

for the low-sensitivity control, indicating that the low-sensitivity trajectories are generally more expensive to follow, at least in this current implementation.

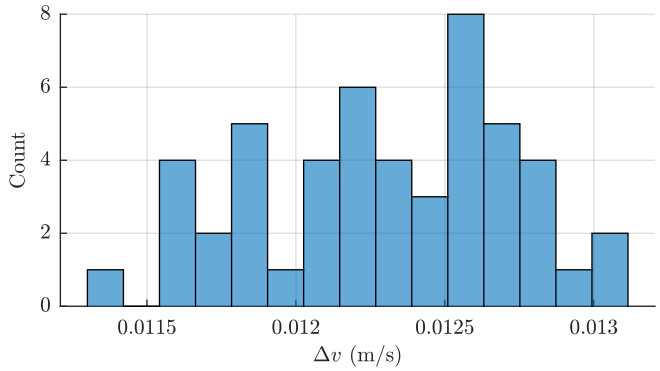

Figure 16. Total Δv (LQR)

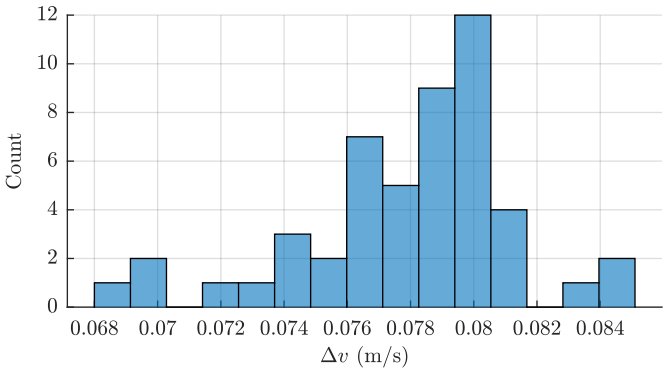

Figure 17. Total Δv (Low-Sensitivity Control)

Figure 18 shows the nonlinearity index vs. time for both controllers. Since this index is meaninglessly inflated as $\Delta \boldsymbol{r}_l \to \mathbf{0}$, the nonlinearity index is only shown while $\|\Delta \boldsymbol{r}_l\| > 0.15$ km. The difference between the two families of curves emphasizes that the low-sensitivity controller follows the expected linear dynamics much more closely, with its nonlinearity index being an order of magnitude lower than for the standard LQR control. The low-sensitivity controller also reduces the scale of the relative motion much more quickly than the standard LQR controller, a feature that cannot be discerned from looking at the trajectories alone.

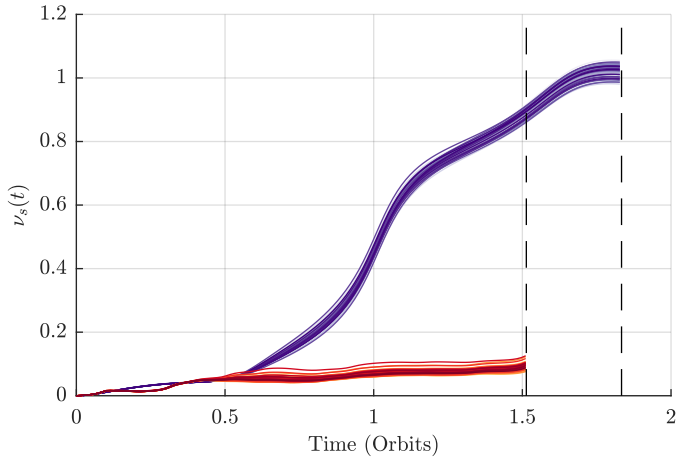

Figure 18. Nonlinearity Index vs. Time, Monte Carlo Results

CONCLUSIONS

In this paper, desensitized control is implemented to solve the formation flying rendezvous problem for spacecraft in orbits about asteroids with uncertain parameters. The method first introduced by Kahne[7] is applied and extended to desensitized control with any number of unknown system parameters. For the example application in this paper, those parameters are C_{20}, C_{22} and the solar radiation pressure (SRP) disturbance magnitude.

Numerical simulations compare the performance and characteristics of the Linear Quadratic Regulator (LQR) control with desensitized control. The desensitized control enables rendezvous along a trajectory that is much closer to the design trajectory predicted by the linearized dynamics. This is an interesting and useful feature for desensitized control, and a surprising result to obtain from a linear control design. The comparative closeness of the design and actual trajectories would be particularly useful for more complex formation control problems, in which operational and geometric constraints would demand that the design trajectory be followed as closely as possible.

There are several topics to explore for future work. First and foremost, the closer agreement between the linear and true trajectories in desensitized control should be investigated. There are also additional applications to be considered. This control strategy could enable the secondary effects of all unknown higher order gravity field components to be compensated for in control design. The resulting control design would be essentially asteroid shape-agnostic. The problem of formation control with a poorly known chief spacecraft orbit could also be studied. The navigation problem around asteroids and other distant bodies is traditionally considered to be a major obstacle for successful multi-spacecraft operations in such environments. However, the desensitized formation control strategy can be used to compensate for the poorly known spacecraft states, so long as the relative position and velocity are measured.

ACKNOWLEDGEMENTS

This work was supported by the U.S. Department of Defense through the National Defense Science and Engineering Graduate Fellowship (NDSEG) Program.

REFERENCES

[1] E. R. Burnett and E. A. Butcher. Linearized Relative Orbital Motion Dynamics in a Rotating Second Degree and Order Gravity Field. In *AAS/AIAA Astrodynamics Specialist Conference*. American Astronautical Society, 2018.

[2] E. R. Burnett and H. Schaub. Spacecraft Formation and Orbit Control Using Attitude-Dependent Solar Radiation Pressure. In *International Workshop on Satellite Constellations and Formation Flying*. IAF Astrodynamics Committee, 2019.

[3] E. R. Burnett and H. Schaub. Study of Highly Perturbed Formation Dynamics Via Approximation. In *International Workshop on Satellite Constellations and Formation Flying*. IAF Astrodynamics Committee, 2019.

[4] S. Casotto. The Equations of Relative Motion in the Orbital Reference Frame. *Celestial Mechanics and Dynamical Astronomy*, 124(3):215–234, 2016.

[5] S. G. Hesar, D. J. Scheeres, and J. W. McMahon. Stability Analysis of the OSIRIS-REx Terminator Orbits to Maneuver Errors. *Journal of Guidance, Control, and Dynamics*, 40(1):81 – 95, January 2017.

[6] M. Kaasalainen and J. Torppa. Optimization Methods for Asteroid Lightcurve Inversion. I. Shape Determination. *Icarus*, 153:24–36, 2001.

[7] Stephen Kahne. Low-Sensitivity Design of Optimal Linear Control Systems. *IEEE Transactions on Aerospace and Electronic Systems*, 4(3):374–379, May 1968.

[8] Christopher D. Karlgaard and Haijun Shen. Desensitized optimal filtering. In *AIAA Guidance, Navigation and Control Conference*, Portland, OR, Aug. 8–11, 2011 2011. Paper AIAA 2011-6617.

[9] J. W. McMahon and D. J. Scheeres. New Solar Radiation Pressure Force Model for Navigation. *Journal of Guidance, Control, and Dynamics*, 33(5):1418–1428, 2010.

[10] D. J. Scheeres. The dynamical evolution of uniformly rotating asteroids subject to YORP. *Icarus*, 188:430–450, 2007.

[11] D. J. Scheeres. *Orbital Motion in Strongly Perturbed Environments*. Springer-Verlag Berlin Heidelberg, 2012.

[12] H. Seywald and R. Kumar. Desensitized optimal trajectories. *Advances in the Astronautical Sciences*, 93:103–106, 1996.

[13] H. Seywald and K. L. Seywald. Desensitized optimal control. *AIAA Scitech Forum*, 2019.